Cellular/Molecular

Histamine Release in the Prefrontal Cortex Excites Fast-Spiking Interneurons while GABA Released from the Same Axons Inhibits Pyramidal Cells

Diana Lucaci,[1] Xiao Yu,[1] Paul Chadderton,[2] William Wisden,[1,3] and Stephen G. Brickley[1]

[1]Department of Life Sciences, Imperial College London, London SW7 2AZ, United Kingdom, [2]School of Physiology, Pharmacology and Neuroscience, University of Bristol, Bristol, United Kingdom, and [3]UK Dementia Research Institute Center at Imperial, Imperial College London, London SW7 2AZ, United Kingdom

We studied how histamine and GABA release from axons originating from the hypothalamic tuberomammillary nucleus (TMN) and projecting to the prefrontal cortex (PFC) influence circuit processing. We optostimulated histamine/GABA from genetically defined TMN axons that express the histidine decarboxylase gene (TMN_{HDC} axons). Whole-cell recordings from PFC neurons in layer 2/3 of prelimbic, anterior cingulate, and infralimbic regions were used to monitor excitability before and after optostimulated histamine/GABA release in male and female mice. We found that histamine-GABA release influences the PFC through actions on distinct neuronal types: the histamine stimulates fast-spiking interneurons; and the released GABA enhances tonic (extrasynaptic) inhibition on pyramidal cells (PyrNs). For fast-spiking nonaccommodating interneurons, histamine released from TMN_{HDC} axons induced additive gain changes, which were blocked by histamine H1 and H2 receptor antagonists. The excitability of other fast-spiking interneurons in the PFC was not altered. In contrast, the GABA released from TMN_{HDC} axons predominantly produced divisive gain changes in PyrNs, increasing their resting input conductance, and decreasing the slope of the input–output relationship. This inhibitory effect on PyrNs was not blocked by histamine receptor antagonists but was blocked by $GABA_A$ receptor antagonists. Across the adult life span (from 3 to 18 months of age), the GABA released from TMN_{HDC} axons in the PFC inhibited PyrN excitability significantly more in older mice. For individuals who maintain cognitive performance into later life, the increases in TMN_{HDC} GABA modulation of PyrNs during aging could enhance information processing and be an adaptive mechanism to buttress cognition.

Key words: **GABA; histamine; hypothalamus; prefrontal cortex**

Significance Statement

The hypothalamus controls arousal state by releasing chemical neurotransmitters throughout the brain to modulate neuronal excitability. Evidence is emerging that the release of multiple types of neurotransmitters may have opposing actions on neuronal populations in key cortical regions. This study demonstrates for the first time that the neurotransmitters histamine and GABA are released in the prefrontal cortex from axons originating from the tuberomammillary nucleus of the hypothalamus. This work demonstrates how hypothalamic modulation of neuronal excitability is maintained throughout adult life, highlighting an unexpected aspect of the aging process that may help maintain cognitive abilities.

Introduction

Histamine, a wake-specific neuromodulator, is produced by tuberomammillary nucleus (TMN) neurons of the posterior hypothalamus (Watanabe et al., 1983; Panula et al., 1984; Haas and Panula, 2003; Scammell et al., 2019; Yoshikawa et al., 2021) that send axons throughout the brain (Takagi et al., 1986; Airaksinen and Panula, 1988; Haas and Panula, 2003; Arrigoni and Fuller, 2021; Yoshikawa et al., 2021) and are defined by expression of the histidine decarboxylase (*hdc*) gene, which encodes the enzyme that synthesizes histamine (Joseph et al., 1990). Histamine is released from axonal varicosities (Takagi et al., 1986) and activates excitatory H1,

Received May 16, 2022; revised Sep. 6, 2022; accepted Nov. 3, 2022.

Author contributions: P.C. and S.G.B. designed research; D.L. and X.Y. performed research; D.L. and S.G.B. analyzed data; D.L., P.C., W.W., and S.G.B. wrote the paper.

This research was funded by the Wellcome Trust (Grant 107841/Z/15/Z, to W.W.), the UK Dementia Research Institute (Grant UK DRI-5004, to W.W.), and the Biotechnology and Biological Sciences Research Council (Grant BB/N008871/1, to P.C and S.G.B.). We retain the right to deposit the accepted manuscript in a repository of their choice and on publication immediately make this manuscript green open access with a CC-BY license.

The authors declare no competing financial interests.

Correspondence should be addressed to Stephen G. Brickley at s.brickley@imperial.ac.uk.

https://doi.org/10.1523/JNEUROSCI.0936-22.2022

H2, and inhibitory H3 metabotropic receptors (Haas and Panula, 2016). As histamine acts by volume/paracrine transmission, it influences multiple elements of the circuitry, fine-tuning both inhibitory and excitatory transmission (Ellender et al., 2011; Bolam and Ellender, 2016). Increased firing of histamine neurons in the TMN is associated with the waking state, and antihistamines that cross the blood–brain barrier cause drowsiness. Therefore, it is expected that histamine release within the neocortex will result in excitation of the cortical circuitry.

Dual transmitter release from a single axonal population is a common phenomenon (e.g., GABA-acetylcholine, GABA-dopamine, and glutamate-orexin release have all been documented; Ma et al., 2018). Similarly, histamine neurons contain GABA as well as the enzyme glutamate decarboxylase GAD1 (GAD67) needed for GABA synthesis (Takeda et al., 1984; Senba et al., 1985; Airaksinen et al., 1992; Trottier et al., 2002). For GABA transport into synaptic vesicles, the VGAT protein (encoded by the *slc32a1* gene) is usually needed (McIntire et al., 1997). Colocalization of *vgat* and *hdc* transcripts (Abdurakhmanova et al., 2020), as well as evidence from *hdc-Cre* × *vgat* reporter mouse crosses (Yu et al., 2015) and visualization of GABA in vesicles of histaminergic cells *in vitro* (Kukko-Lukjanov and Panula, 2003), suggested GABA release from vesicles in histamine neurons (Ma et al., 2018). Indeed, we found that in the visual cortex histaminergic axons broadcast both GABA and histamine (Yu et al., 2015).

As well as causing fast (millisecond) synaptic inhibition through $GABA_A$ receptors, GABA can diffuse to extrasynaptic ionotropic $GABA_A$ receptors to produce a tonic shunting inhibition (Brickley et al., 1996; 2001; Wall, 2002; Brickley and Mody, 2012; Lee and Maguire, 2014; Brickley et al., 2018). Knockdown of *vgat* in *hdc* cells enhanced the activity of mice and reduced their sleep. In the visual cortex, light-evoked GABA release increased tonic inhibition in pyramidal cells, which was diminished when *vgat* gene expression was knocked down (Yu et al., 2015). Therefore, our work has challenged the view that the influence of histaminergic neurons on cortical circuitry will be purely excitatory.

vgat expression in histaminergic cells has become controversial, however. Combined immunocytochemistry and *in situ* hybridization for HDC protein and *vgat* mRNA revealed little coexpression (Venner et al., 2019), but single-cell RNA-sequencing (seq) studies of mouse TMN identified a subset (E5) of *hdc* cells with moderate expression of *vgat* (Mickelsen et al., 2020). This subset of cells, because of their long-range projections, could still have widespread influence. Therefore, in this study we have extended our analysis to the prefrontal cortex (PFC) and broadened our investigation to assay excitability changes in pyramidal cells and interneurons. We have used whole-cell recording techniques combined with optogenetics to describe how the gain of the input–output (I-O) relationship is altered following GABA/histamine release from hdc-expressing TMN axons (TMN_{HDC} axons). Importantly, we have now recorded over a much broader age range than in our previous study (Yu et al., 2015) to ask whether the changes in excitability associated with GABA/histamine release are uniform across the adult life span. For the first time, we show that GABA release is elicited from genetically defined histaminergic axons in the PFC of young and old mice (of both sexes) and that the GABA/histamine cotransmission works together to enhance pyramidal cell information transfer, especially in older animals.

Materials and Methods

Mice. All procedures were performed in accordance with the United Kingdom Home Office Animal Procedures Act (1986) and were approved by the Imperial College Ethical Review Committee. The strains of mice used were HDC-Cre ($Hdc^{tm1.1(icre)Wwis/J}$; stock #021198, The Jackson Laboratory; Zecharia et al., 2012) and Pv-Cre ($Pvalb^{tm1(cre)Arbr/J}$; stock #008069, The Jackson Laboratory) (Hippenmeyer et al., 2005). The *HDC-Cre* mouse line contains an *ires-Cre* cassette knocked in to exon 12 of the *hdc* gene. The insertion is downstream of the stop codon for the *hdc* reading frame, and therefore the knock-in allele makes HDC and Cre proteins (Zecharia et al., 2012).

AAV vectors and surgery. Adeno-associated viruses (AAVs; capsid serotype 1/2) were packaged in-house and contained either an *AAV-EF1a-flex-ChR- ChR2H134R-EYFP* transgene (plasmid 20298, Addgene; a gift from Karl Deisseroth; James H. Clark Center, Stanford University, California) or an *AAV-CBA-flex-GFP* transgene (plasmid 28304, Addgene; a gift from Edward Boyden; Massachusetts Institute of Technology, Cambridge, MA). To deliver the *AAVs* into the brain, bilateral stereotaxic injections were performed on *HDC-Cre* or *Parv-Cre* mice using an Angle Two apparatus (Leica) linked to a digital brain atlas (Leica Biosystems). Before injections, 1 μl of AAV virus was mixed with 1 μl of 20% mannitol (catalog #K93152782111, MERCK). The virus and mannitol mixture was injected into a pulled-glass pipette (Warner Instruments; outer diameter, 1.00 mm; inner diameter, 0.78 mm; length, 7.5 cm). Virus was injected at a speed of 25 nl/min. Virus (1 μl) was bilaterally injected into the brain, 0.5 μl for each side. For the TMN, the injection coordinates were as follows: mediolateral (ML), −0.92 mm; anteroposterior (AP), −2.70 mm; dorsoventral (DV), −5.34 mm; ML, 0.92 mm; AP, −2.70 mm; and DV, −5.34 mm (Yu et al., 2015). For the frontal cortex the coordinates were as follows: ML, 0.33 mm; AP, 2.10 mm; DV, −2.13 mm; 0.3 µl of virus was injected.

After each injection, pipettes were left undisturbed for 10 min to allow the viral solution to be absorbed by the tissue; thereafter, pipettes were removed slowly. After injection, craniotomies were sealed with Kwik-Cast (World Precision Instruments), and the scalp was sutured with glue (Histoacryl, Braun) or nonabsorbable nylon sutures (Ethilon, Ethicon). Immediately after suturing, anesthesia was antagonized via injection of a naloxone, flumazenil, and atipamezole mixture (1.2, 0.5, and 2.5 mg/kg, i.p.). Postoperative analgesia was provided via application of eutectic mixture of local anaesthetics (2.5% lidocaine and prilocaine) to the sutured skin. Mice were placed in a heated recovery box under observation until they fully woke up from anesthesia; thereafter, animals were returned to their home cage. Four to 5 weeks after the AAV injection, we prepared acute slice preparations containing the TMN area. If there was visible primary fluorescence in this area, we also went on to slice the PFC. Initially, we also tested for the presence of channelrhodopsin-2 (ChR2) by patching the cells fluorescent TMN cells and in current-clamp mode and by eliciting an inward current response with blue light stimulation of ChR2 to confirm the presence of functional ChR2. Slices from TMN injections that gave no visible primary expression were discarded or used as negative controls.

PFC slice electrophysiology. Acute brain slices were prepared from male and female mice following cervical dislocation. Each mouse brain was rapidly removed from the cranium and immediately immersed in ice-cold, oxygenated slicing solution. The slicing solution contained the following (in mM): NMDG 92, KCl 2.5, NaH_2PO_4 1.25, 30 mM NaHCO3, HEPES 20, glucose 25, thiourea 2, Na-ascorbate 5, Na-pyruvate 3, $CaCl_2 \cdot 4H_2O$ 0.5, and $MgSO_4 \cdot 7H_2O$ 10, at pH 7.3–7.4 when bubbled with 95%O_2/5%CO_2 and titrated with concentrated hydrochloric acid. Acute slice preparations were cut using a vibratome (Campden Instruments) at a thickness of 250 μm, after which they were immediately transferred to a holding chamber containing slicing ACSF at 33–34°C continuously bubbled with 95%O_2/5%CO_2, and slices were kept in this condition for 10–15 min, after which they were transferred into a holding chamber at room temperature containing the following recording ACSF (in mM: NaCl 125, KCl 2.5, $CaCl_2$ 2, $MgCl_2$ 1, NaH_2PO_4 1.25, $NaHCO_3$ 26, and glucose 11, at pH 7.4 when bubbled with 95%O_2/5%CO_2) that was continuously bubbled with 95%

O_2/5%CO_2. Slices were then visualized using a fixed-stage upright microscope (model BX51W1, Olympus; and SliceScope, Scientifica) fitted with a high numerical aperture water-immersion objective and an infrared-sensitive digital camera. Patch pipettes were made from thick-walled borosilicate glass capillaries (internal diameter, 0.86 mm; outer diameter, 1.5 mm; Harvard Apparatus) using a two-step vertical puller (PC-10, Narishige). Pipette resistances were typically 3–4 MΩ when back-filled with internal solution. For voltage-clamp experiments, the internal solution contained the following (in mM): CsCl 140, NaCl 4, $CaCl_2$ 0.5, HEPES 10, EGTA 5, and Mg-ATP 2; the pH was adjusted to 7.3 with CsOH. For current-clamp experiments the internal solution contained the following (in mM): 145 K-gluconate, 4 NaCl, 0.5 $CaCl_2$, 10 HEPES, 5 EGTA, 4 Mg-ATP, and 0.3 Na-GTP, adjusted to pH 7.3 with KOH. The amplifier head stage was connected to an Axopatch 700B amplifier (Molecular Devices). The amplifier current output was filtered at 10 kHz (−3 dB, eight-pole low-pass Bessel filter) and digitized at 20 kHz using a digitization board (models NI-DAQmx, PCI-6052E, National Instruments). Data acquisition was performed using a CED Power3 1401 processor and CED Signal (version 6) software.

Optogenetics. A 470 nm collimated LED (catalog #M470L3-C1, Thorlabs) was used to illuminate the slice through the objective lens. The LED was driven by an LED-driver (model LEDD1B, Thorlabs), which was controlled by a digitization board (models NI-DAQmx, PCI-6052E, National Instruments). The output of the LED was measured with a power meter (model PM100D, Thorlabs) positioned below the objective lens, and the power output and membrane conductance or voltage changes were aligned for analysis. The optical power emitted through our 63× water-immersion lens increased linearly to a maximum power of 70 mW/mm^2 at our chosen light stimuli, giving rise to a transient response that peaked at 40 mW/mm^2, with a 10–90% rise time of 0.73 ms and a decay constant of 9.65 ms.

Data analysis. For all recorded cells, total membrane capacitance (C_m) was calculated in voltage-clamp configuration from $C_m = Q/\Delta V$, where Q was the charge transfer during a hyperpolarizing 10 mV step of the command voltage (ΔV). The total membrane conductance (G_m) was calculated from $G_m = I_{ss}/\Delta V$, where I_{ss} was the average steady-state current during the ΔV. The electrode-to-cell series resistance (R_s) was calculated from the relationship $R_s = \Delta V/I_p$, where I_p was the peak of the capacitive current transient and recordings were excluded if R_s increased by >30%.

Experimental design and statistical analysis. To test for statistical significance between single-cell properties across our broad range of ages, we first applied the Mann–Whitney nonparametric test. We then applied the Benjamini–Hochberg (B-H) correction at $p = 0.05$ and 0.01 values to control for multiple comparisons. As we were looking for changes in many biophysical properties, we chose the B-H correction procedure as it is less sensitive than the Bonferroni procedure to decisions about the identity of a "family" of tests. Briefly, the B-H procedure ranks individual p-values and then compares individual p-values to their B-H critical value, $(i/m) * Q$, where i is the rank, m is the total number of tests, and Q is the false discovery rate. The largest p-value that has $p < (i/m) * Q$ is considered significant.

Results

Four to 5 weeks before whole-cell recording experiments, an AAV containing a flex-ChR2-EYFP transgene was delivered into the TMN of HDC-Cre mice (Fig. 1*A*). The expression of ChR2-EYFP (enhanced yellow fluorescent protein) was verified in the TMN (Fig. 1*B*), and, like our previous reports, we found that ChR2-EYFP expression was restricted to a subset of hdc-expressing neurons of the TMN (Fig. 1*C*). Whole-cell recordings were then made from fast-spiking interneurons (FS-INs) and pyramidal neurons (PyrNs) within layer 2/3 of the prelimbic (PL), anterior cingulate (AC), and infralimbic (IL) regions of the PFC (Fig. 1*D*). Following these recordings, the presence of fluorescently labeled TMN_{HDC} axons was observed in the PFC (Fig. 1*E*). 3D reconstructions of biocytin-filled cells in the PFC demonstrated how these fluorescently labeled TMN_{HDC} axons rarely make close appositions (<1 μm) with PyrN dendrites (Fig. 1*F*), as expected from previous studies (Takagi et al., 1986). PyrNs, fast-spiking accommodating FS-INs ($FS\text{-}IN_a$s), and nonaccommodating FS-INs ($FS\text{-}IN_{na}$s) in layer 2/3 were selected according to their location, soma shape, and electrophysiological features. Most strikingly, PyrNs exhibited evoked AP firing rates of <20 s, with an average maximum AP rate of 11.4 ± 0.5 s ($n = 19$), whereas the evoked firing rates of FS-INs was between 20 and 90 s with an average maximum AP rate of 46.6 ± 3.8 s ($n = 19$; Fig. 1*G*). To further confirm the identity of FS-INs, we patched green fluorescent protein (GFP) fluorescent cells from PV-Cre mice following AAV-flex-GFP injection into the PFC ($n = 4$). As expected, AP characteristics for the parvalbumin-expressing cells were like those observed in the FS-IN group. A further breakdown of the FS-IN group was based on differences in the interspike intervals (ISIs) of FS-INs (Fig. 1*H*). Cells with stable ISIs were classified as $FS\text{-}IN_{na}$s, whereas fast-spiking cells with an unstable ISI were classified as $FS\text{-}IN_a$s. This variability score was close to zero for $FS\text{-}IN_{na}$ cells (Fig. 1*I*), and there was no overlap with the ISI variability in the $FS\text{-}IN_a$ population ($FS\text{-}IN_a$ = 11; $FS\text{-}IN_{na}$ = 15; $p < 1.3E\text{-}7$ by a Mann–Whitney U test). The regular fast-spiking interneuron population ($FS\text{-}IN_{na}$s) could contain basket, chandelier, and neurogliaform cell types that all provide axosomatic feedforward and feedback inhibition onto PyrNs (Feldmeyer et al., 2018). Based on firing properties alone, the irregular spiking population ($FS\text{-}IN_a$s) are likely to represent the somatostatin-positive Martinotti and non-Martinotti cells that target inhibition to the basal and apical dendrites of PyrNs (Feldmeyer et al., 2018). However, additional morphologic and immunohistochemical analysis would be required to confirm this classification (Krimer et al., 2005).

Optogenetic stimulation of TMN_{HDC} axons alters excitability in the PFC

During whole-cell recording, TMN_{HDC} fibers in the PFC slices were activated with 1 ms duration blue light flashes delivered at a rate of 5 s every 0.4 s for a total stimulation period of 4 min (Yu et al., 2015). This protocol was chosen to mimic the short 5 s AP bursts that have been observed for several minutes when recording from wake-active TMN neurons during attentive waking in mice (Takahashi et al., 2006). In the example shown in Figure 2*A*, simultaneous whole-cell recordings were made from a $FS\text{-}IN_{na}$ and a PyrN. In PyrNs, a reduction in AP firing rates following TMN_{HDC} axon stimulation was obvious from the I-O relationships constructed from average AP rates. As shown in Figure 2, *B* and *C*, the I-O relationships for data obtained from an individual PyrN (Fig. 2*B*) and an $FS\text{-}IN_{na}$ (Fig. 2*C*) could be well described by a sigmoidal function, both before and after optogenetic stimulation. Results from the fits obtained from 19 PyrNs were pooled, and the average I-O relationship before and after optogenetic stimulation of TMN_{HDC} axons was constructed (Fig. 2*D*). This analysis demonstrated that the maximum AP firing rate was reduced from 12.7 ± 1.6 to 3.9 ± 5.3 s following stimulation of TMN_{HDC} axons (Wilcoxon signed-rank test, $p = 0.0002$). The slope of the average I-O relationship significantly reduced from 7.6 ± 0.9 to 2.4 ± 0.7 (Wilcoxon signed-rank test, $p = 0.0004$) with no significant reduction in the current required to reach 50% of the maximum AP rate (before stimulation, 50.4 ± 36.2 pA; after stimulation, 49.9 ± 18.9 pA; Wilcoxon signed-rank test, $p = 0.7$). Transforming the average, the I-O relationship obtained under control conditions with a purely divisive function indicates that an additive gain change mechanism may make a minor contribution

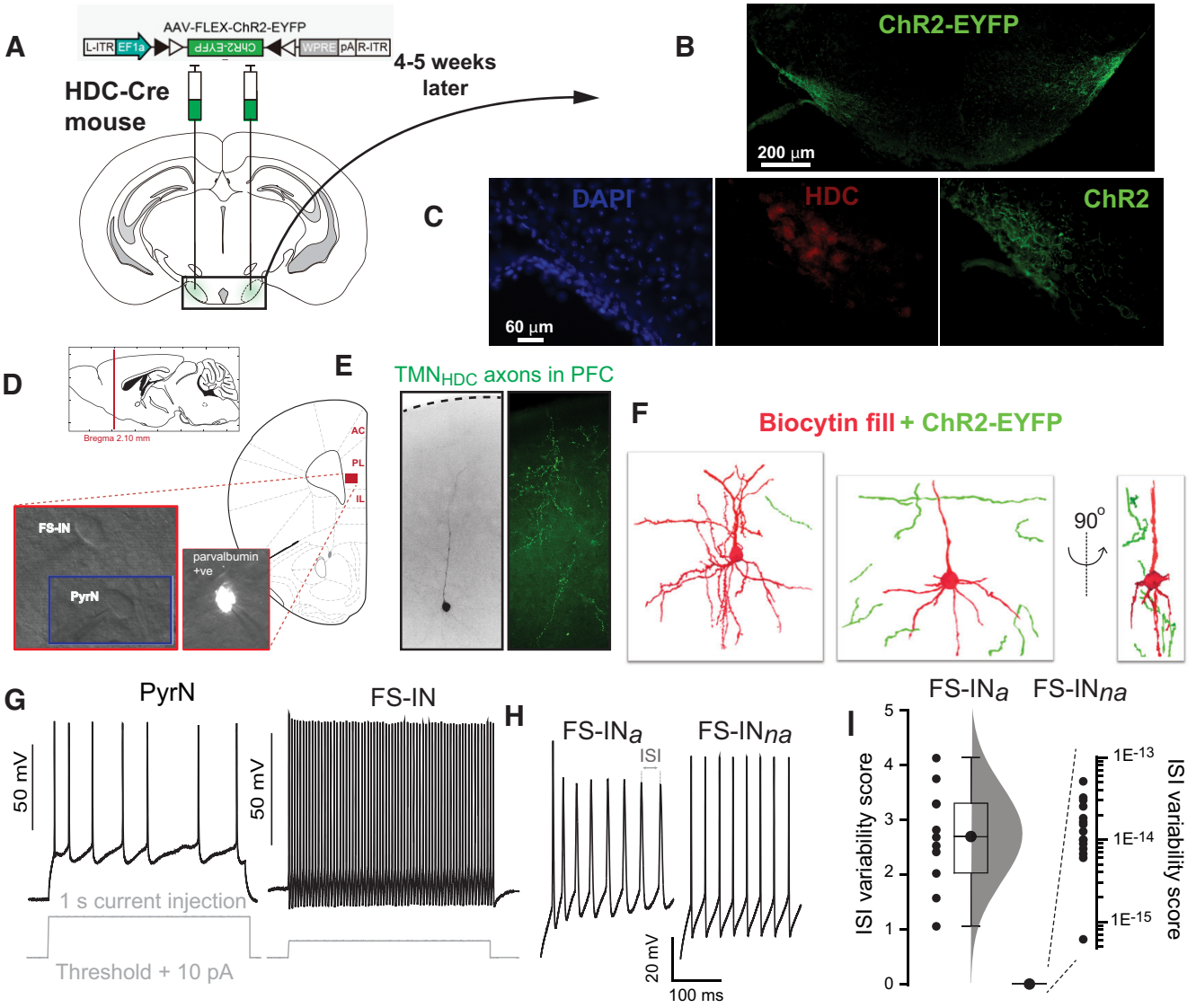

Figure 1. Targeting of ChR2-EYFP expression to TMN axons and identification of neuronal types in the PFC. ***A***, Depiction of the construct used to target ChR2-EYFP expression to neurons of the TMN in the HDC-Cre mouse strain. The location of bilateral AAV injections is shown superimposed on an image taken from the Allen Brain Atlas. ***B***, Low-magnification epifluorescent image of a coronal brain section taken 4–5 weeks after AAV injection demonstrating EYFP expression in the TMN. ***C***, Higher-magnification image of all cell bodies present in the TMN on one side of the brain using a nuclear DAPI stain (blue) and a comparison with histamine-expressing neurons identified using the HDC antibody (red) and the ChR2-expressing neurons labeled as in ***B***. ***D***, Illustration of the PFC region where, 4–5 weeks later, blue light was delivered through a high-numerical aperture imaging objective to stimulate ChR2. Included in this panel is a sagittal location of the mouse PFC along with a coronal section showing the three areas of the PFC where recordings were made: AC, PL, and IL. The illustrations were adapted from the Allen Mouse Brain Atlas. Bright-field images were taken during whole-cell recording, and the fluorescent cell was recorded from the Parv-Cre mouse following flexed-GFP delivery into the PFC. ***E***, Microscope images taken from the PFC region where recordings were made and blue light was delivered. The left-hand bright-field image demonstrates the location of the biocytin-filled PFC neuron, and the epifluorescent image on the right illustrates the presence of ChR2-EYFP-labeled axon terminals in this region of the PFC. ***F***, PFC neurons were reconstructed following confocal microscopy to reveal the proximity of the TMN axons relative to the recorded neuron. As expected, the ChR2-EYFP-labeled axon terminals were never observed closely enough (<1 µm) to indicate the presence of conventional synaptic connections. ***G***, Examples of voltage recordings made in whole-cell current-clamp configuration during steady-state 1 s current injections sufficient to elicit APs. A representative voltage trace is shown from a PyrN and an FS-IN. ***H***, Comparison of FS-IN$_a$ and FS-IN$_{na}$ firing. ***I***, Plot of the ISI changes for the two recordings shown in ***H***. Comparison of ISI analysis standardized to zero mean and 1 SD. The sum of the standardized ISI is referred to as the "ISI variability score." This score is extremely close to zero for the FS-IN$_{na}$ group, hence the logarithmic scale. No overlap between the groups is observed. The difference in ISI score is significant to $p < 0.01$ using Mann–Whitney and Benjamini–Hochberg corrections.

to changes in PyrN excitability. Specifically, there was a small leftward shift in the current required to reach AP threshold that was not predicted from a purely divisive model (Fig. 2*D*). However, the most striking aspect of the changes in the I-O relationships constructed from PyrN recordings were the divisive effects observed following TMN$_{HDC}$ axon stimulation.

The average firing rates of the FS-IN$_{na}$ population ($n = 8$) significantly increased following optogenetic stimulation of TMN$_{HDC}$ axons (Fig. 2*E*). The change in the average I-O relationship of the FS-IN$_{na}$ population was consistent with an additive gain change mechanism (Fig. 2*E*). The maximum AP firing rate increased from 39.8 ± 3.8 to 44.8 ± 3.8 s (Wilcoxon signed-rank test, $p = 0.008$) with 50% excitation point shifting from 82.4 ± 17.8 to 70.0 ± 16.2 pA (Wilcoxon signed-rank test, $p = 0.5$). However, there was also a small but significant reduction in the slope of the input–output relationship from 0.3 ± 0.2 to 0.2 ± 0.1 (Wilcoxon signed-rank test, $p = 0.008$). Therefore, like the situation for PyrNs, analysis of I-O relationships suggests that two types of gain mechanism could operate within the FS-IN$_{na}$ population. However,

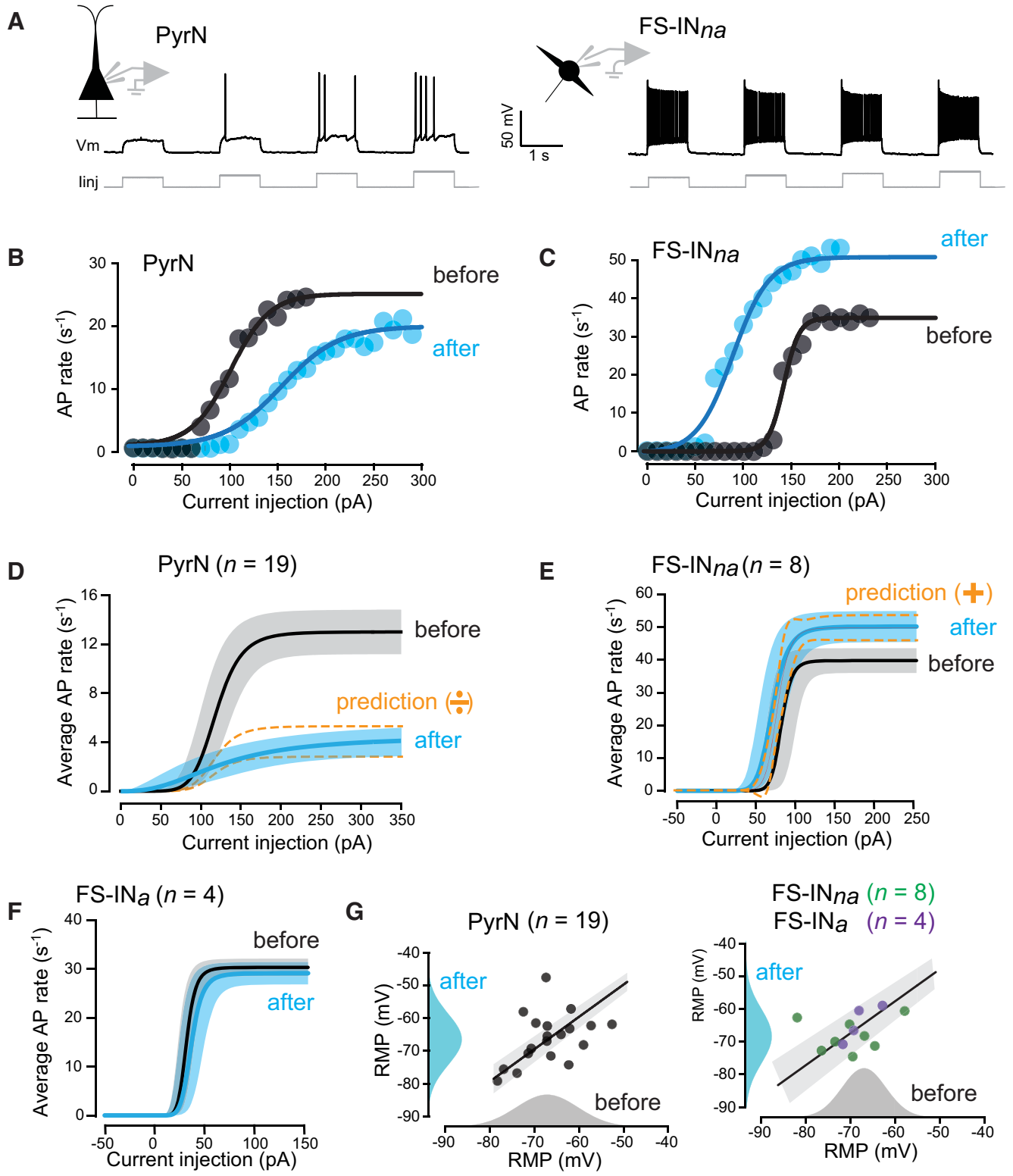

Figure 2. Optogenetic release of GABA/Histamine from axons within the adult PFC. ***A***, Voltage traces obtained during simultaneous whole-cell recording from a PyrN and an FS-IN_{na} used to monitor changes in AP firing. ***B***, A representative example of the fit obtained for a single PyrN before and after optogenetic stimulation of the TMN_{HDC} axon terminals. ***C***, A representative example of the fit obtained for a single FS-IN_{na} before and after optogenetic stimulation of the TMN_{HDC} axon terminals. ***D***, Comparison of the average fits obtained from the input–output relationships constructed from the PyrN population ($n = 19$) before and after optogenetic stimulation of the TMN_{HDC} axon terminals in the PFC. The solid black line is the average fit with the gray-shaded area showing the 95% confidence limits for the fits obtained before stimulation. The solid blue line is the average fit, and the shaded blue region show the 95% confidence limits for fits obtained after optogenetic stimulation. The dashed lines demonstrate the predictions when assuming a purely divisive gain change mechanism in PyrNs. ***E***, Comparison of the average fits obtained from the input–output relationships constructed from the FS-IN_{na} population ($n = 8$) before and after optogenetic stimulation of the TMN_{HDC} axon terminals in the PFC. In contrast to the data from PyrNs, an additive gain-change mechanism was solely responsible for the increased firing observed in the FS-IN_{na} population. ***F***, Comparison of the average fits obtained from the input–output relationships constructed from the FS-IN_a population ($n = 4$) before and after optogenetic stimulation of the TMN_{HDC} axon terminals in the PFC. Note the lack of any change in the FS-IN_a population. ***G***, Scatter plots for the RMP recorded before and after optogenetic stimulation in PyrNs and FS-INs with the results of linear region analysis. The all-point histograms

transforming fits from the FS-IN_{na} population solely with an additive function predicted well the changes observed in the I-O relationship.

In contrast to the clear changes observed for PyrNs and FS-IN_{na}s, the excitability of the FS-IN_a population was unchanged following optogenetic stimulation of TMN_{HDC} axons in the PFC ($n = 4$), such that the maximum AP rate was 30.4 ± 1.8 s before stimulation and 29.2 ± 2.2 s after. There was also no significant change in the slope of the I-O relationship (6.8 ± 1.4 vs 6.4 ± 1.4) or the current required to reach 50% of the maximum AP rate (28.2 ± 7.1 vs 32.9 ± 11.1 pA) in the FS-IN_a population (Fig. 2*F*).

Consistent with an additive gain change mechanism, neither the resting membrane potential (RMP) nor the input conductance of the FS-IN_{na} population was altered following stimulation of TMN_{HDC} axons (Fig. 2*G*). The resting membrane potential of the PyrN population was also not altered during the tonic shunting inhibition associated with this divisive gain change. However, consistent with a divisive gain change mechanism, there was a significant 20% increase in membrane conductance in PyrNs following optogenetic stimulation that was consistent with a shunting inhibition (see Fig. 5*F*; $n_{pyr} = 22$, $p < 0.02$ using a paired-sample Wilcoxon signed-rank test). The divisive gain change observed in PyrNs is consistent with GABA binding to extrasynaptic $GABA_A$ receptors, whereas the additive gain change associated with the FS-IN_{na} population is more likely to be because of modulation of excitability following the action of histamine on G-protein-coupled receptors. To test this hypothesis, we next undertook some simple pharmacological experiments, during which the time course of the gain change was also examined.

The PyrN divisive gain change involves $GABA_A$ receptors

To compare the time course associated with changes in PyrN excitability the average AP rate was calculated during the entire depolarizing current injection protocol (Fig. 3*A*). The subthreshold membrane voltage appeared more linear following TMN_{HDC} axon activation and in 10 of 22 PyrNs tested, no APs could be elicited following optogenetic stimulation. However, with larger depolarizing currents, AP firing was possible in these PyrNs (data not shown). Simple Boltzmann functions fitted to the time course plots demonstrated that the reduction in PyrN firing was apparent at 2–3 min following TMN_{HDC} axon activation (Fig. 3*B*). Analysis of all fits demonstrated that the average AP rate reduced significantly from 10.7 ± 0.8 to 4.5 ± 0.9 s following optogenetic stimulation ($n = 22$) and the average change in the AP rate for this group was −65.7 ± 8.4%. Several negative control experiments were conducted with acute PFC slices from *HDC-Cre* mice ($n = 8$) that had not received *AAV-flex-ChR2* injections into the TMN. In these experiments, the optogenetic protocol resulted in a −15.9 ± 7.0% change in AP firing rates in PyrNs that was not significant ($n = 8$; $p < 0.06$, Wilcoxon signed-rank test). There was also no change in resting membrane potential or membrane conductance in these PyrNs. As a further control, the addition of the $GABA_A$ receptor antagonist SR95531 blocked the actions of TMN_{HDC} axon stimulation, resulting in only a small reduction in AP firing rates in PyrNs of −7.7 ± 10% following optogenetic stimulation that was also not significant ($n_{H1,H2} = 5$, $n_{GABAA} = 5$; $p < 0.029$, Mann–Whitney *U* test).

Pharmacological experiments were undertaken to directly address the involvement of H1/H2 receptors in the gain change. The optogenetic experiments described above were repeated in the presence of H1 (pyrilamine) and H2 (ranitidine) receptor antagonists. Immediately after the TMN_{HDC} axon stimulation protocol, a larger depolarizing current was required to elicit APs in PyrNs (Fig. 3*C*), and, on average, the AP firing rate in PyrNs decreased by −70.0 ± 15.8% in the presence of H1/H2 antagonists ($n = 5$; $p < 0.032$, Wilcoxon signed-rank test). In the example shown in Figure 3*C*, the average AP rate was 6.4 s before blue light stimulation, but was zero following stimulation. Therefore, in this PyrN the cell excitability was considered to have been reduced by −100% (Fig. 3*D*). Clear changes in the subthreshold voltage behavior of this PyrN was still observed following TMN_{HDC} axon stimulation. The net inhibition of PyrNs observed following TMN_{HDC} axon stimulation in the PFC was −65.7 ± 8.4% ($n = 22$) in control conditions compared with −70.0 ± 15.8% ($n = 5$) in the presence of H1/H2 antagonists. A similar fast time course for PyrN AP firing rate changes were also observed in the presence of the H1/H2 blockers.

The FS-IN_{na} additive gain change involves histamine receptors

Once again, the excitability of the FS-IN_a population was unchanged following optogenetic stimulation of TMN_{HDC} axons in the PFC, but the FS-IN_{na} population became more excitable (Fig. 4*A*). In this example, the average AP rate increased from 10.6 to 171.7 s, and this additive gain change was not associated with any change in the resting input conductance, as evidenced by the linear subthreshold *I–V* relationship before and after stimulation of TMN_{HDC} axons. The time course plots demonstrated that the enhancement of FS-IN_{na} firing was noticeably delayed relative to the end of the blue light stimulation (Fig. 4*B*) with the increase in AP rate occurring 10 min after the end of blue light stimulation at a much slower rate than that apparent for the reduction in PyrN excitability. This slow time course of the increase in AP firing could reflect a more gradual increase in histamine concentrations in the extracellular space or a mechanism involving modulation by G-protein-coupled receptors such as the H1/H2 receptors, whereas the rapid time course of the reduction in AP firing in PyrNs is consistent with the rapid binding of GABA to high-affinity ligand-gated ion channels. To examine the contribution of H1/H2 receptors in the additive gain change the optogenetic experiments described above were repeated in the presence of H1 (pyrilamine) and H2 (ranitidine) receptor antagonists. With histamine receptors blocked there was no change in the average AP rate after the TMN_{HDC} axon stimulations (Fig. 4*C*), and, on average, the AP firing rate in the FS-IN_{na} population was not increased in the presence of H1/H2 antagonists (Fig. 4*D*).

Age differences associated with TMN_{HDC} modulation of the PFC

We next explored the age dependence of TMN_{HDC} modulation of the PFC. First, we examined whether there were any age-related or sex-related differences in the resting input conductance of PyrNs. As shown in Figure 5*A*, the resting input conductance of PyrNs was similar across the adult life span, and this parameter was not influenced by the sex of an

←

constructed before and after optogenetic stimulation further demonstrates how the RMP does not alter. The straight lines are the results of linear regression analysis, with the 95% confidence limits shown in gray-shaded areas.

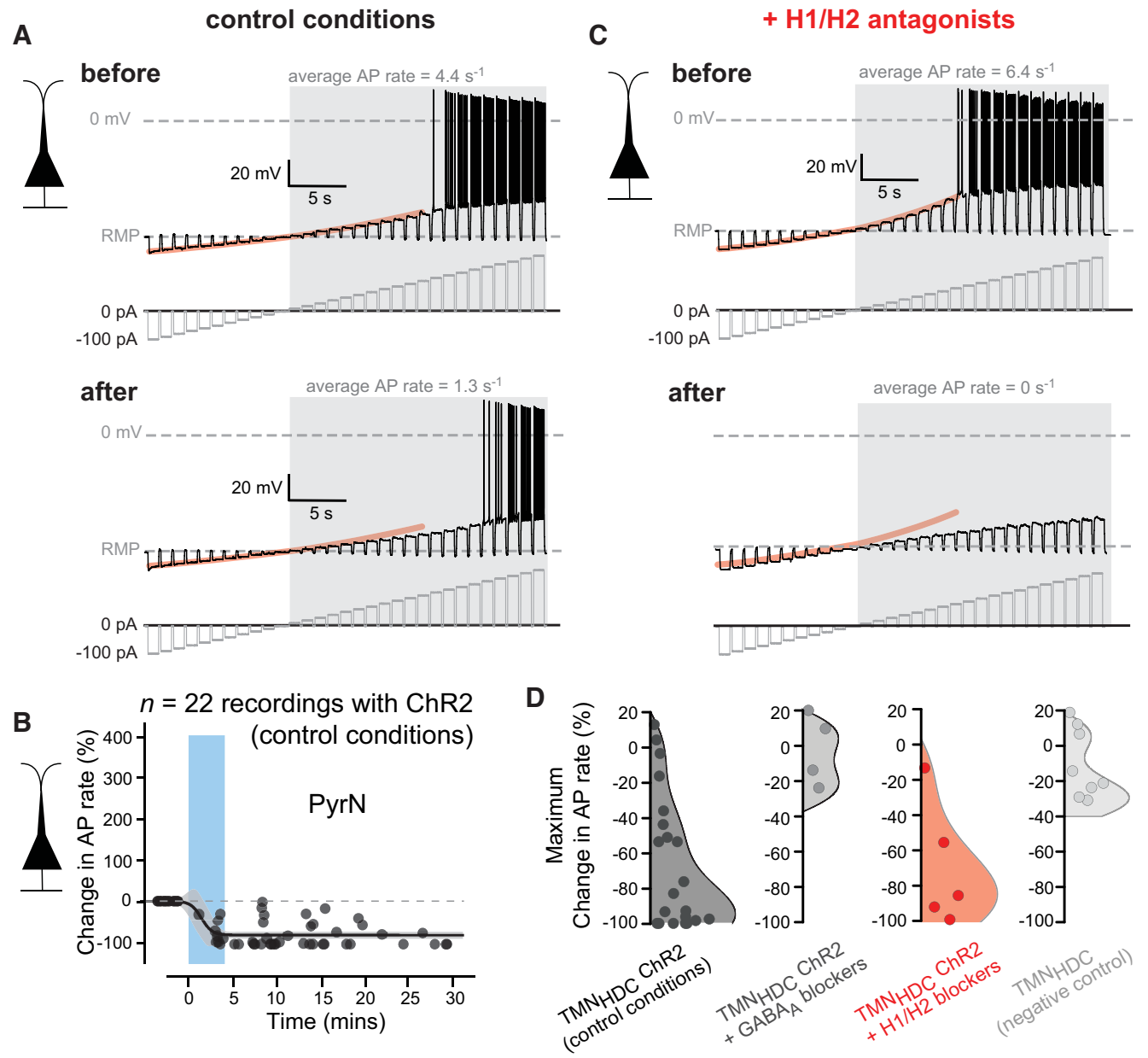

Figure 3. The effect of blocking H1/H2 receptors on changes in the excitability of the PyrNs in the PFC. ***A***, Voltage traces recorded from a PyrN before and after optogenetic stimulation of TMN_{HDC} axons. The current injection protocols are shown below each voltage trace in gray. The average AP rate was calculated during the shaded epoch of the recording following threshold crossing at 0 mV. The subthreshold membrane–voltage relationship obtained before blue light stimulation is highlighted in orange and superimposed onto the voltage response recorded after blue light stimulation for comparison. In this case, the subthreshold *I–V* relationship becomes more linear following light stimulation. ***B***, Plots illustrating the change in average AP rate following optogenetic stimulation of the TMN_{HDC} axons. The time course of changes in average AP rate were described using a Boltzmann function to quantify the rate as well as the magnitude of the change in excitability. The shaded area indicates the 95% confidence limits for these fits. ***C***, Same conventions as in ***A***, but the data were obtained from PyrNs in the presence of H1/H2 antagonists. Note in ***C*** how the subthreshold response of PyrNs becomes more linear following optogenetic stimulation of TMN_{HDC} axons. ***D***, Combined scatter and violin plots illustrating the change in AP rate in control conditions with the expression of ChR2 in TMN_{HDC} axons (black symbols), with $GABA_A$ receptors blocked (dark gray symbols) and with H1/H2 blockers (red symbols). The final plot illustrates the results of a negative control experiment performed in the absence of ChR2 in TMN_{HDC} terminals (light gray symbols).

animal. A linear regression analysis of these data (male and female) resulted in a negative slope and a Pearson's correlation coefficient or r^2 of −0.03, demonstrating how variability in the resting input conductance was not significantly influenced by the age of the animal (ANOVA, $p = 0.72$). Across the entire life span, the resting input conductance of the PyrNs recorded from male mice was 4.44 ± 0.36 nS ($n = 55$) compared with 5.44 ± 0.47 nS ($n = 46$) for female mice. Much of the variability observed for the resting input conductance in the PyrN population (4.90 ± 0.36 nS; $n = 101$) was expected to be explained by variability in cell size as determined from the membrane capacitance (39.1 ± 3.6 pF). Therefore, a least-squares regression analysis (Fig. 5*B*) of the normalized data demonstrates a slope of +0.34 with an r^2 value of 0.37, indicating that nearly 40% of the variability in the input conductance (PC2) can be explained by differences in cell size (PC1). Hypothesis testing using ANOVA demonstrated how the slope of this relationship was significantly greater than zero ($p = 0.0003$). Next, we looked for changes in the response of PyrNs to GABA/histamine release from TMN_{HDC} axons across the adult life span by plotting the change in AP rate as a function of age for PyNs (Fig. 5*C*; $n = 20$). A simple regression analysis of

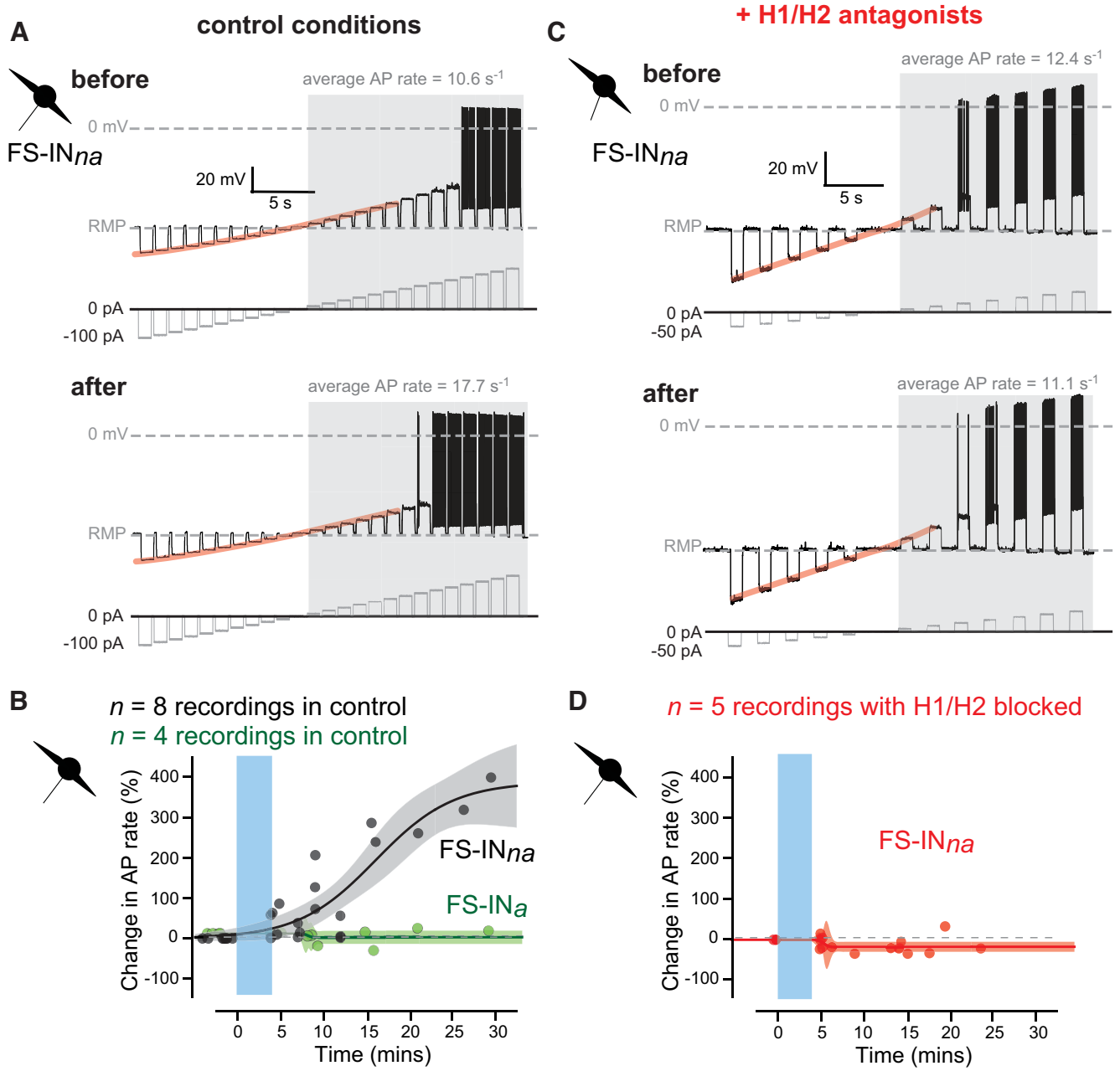

Figure 4. The effect of blocking H1/H2 receptors on changes in the excitability of the FS-IN$_{na}$ population in the PFC. ***A***, Voltage traces recorded from an FS-IN$_{na}$ before and after optogenetic stimulation of TMN$_{HDC}$ axons. The current injection protocols are shown below each voltage trace in gray. The average AP rate was calculated during the shaded epoch of the recording following threshold crossing at 0 mV. The subthreshold membrane–voltage relationship obtained before blue light stimulation is highlighted in orange and superimposed onto the voltage response recorded after blue light stimulation for comparison. In this case, the subthreshold response does not change following light stimulation. ***B***, Plots illustrating the change in average AP rate in the FS-IN$_{na}$ population (black symbols) and the FS-IN$_{a}$ population (green symbols). The time course of these changes in average AP rate in the FS-IN$_{na}$ population can be described using a Boltzmann function, and the shaded area indicates the 95% confidence limits for these fits. ***C***, ***D***, Same conventions as in ***A*** and ***B***, but the data were obtained from the FS-IN$_{na}$ population in the presence of H1/H2 antagonists. Note in ***C*** how the subthreshold *I–V* relationship of FS-INs does not alter following optogenetic stimulation of TMN$_{HDC}$ axons, and how in ***D*** there is no increase in AP rate following stimulation.

these data demonstrated that the magnitude of this inhibition increased as a function of age with a slope of −0.03 and an r^2 value of −0.45, indicating that nearly 50% of the variability in TMN$_{HDC}$ modulation can be explained by age. Furthermore, ANOVA demonstrated that at the $p < 0.05$ level, the slope of this relationship was significantly different from zero ($p = 0.045$). Therefore, TMN$_{HDC}$ axon modulation of PyrN excitability is maintained throughout the adult life span with a tendency to increase with age.

We repeated this analysis for the two interneuron populations we have recorded in the mouse PFC. The resting input conductance of all FS-INs ($n = 23$ recordings) was not related to the age of the mouse (Fig. 5*D*) with no correlation observed in the data ($r^2 = 0.02$; ANOVA, $p = 0.58$). Although the number of recordings in each group was small, the resting input conductance of FS-IN$_{na}$ and FS-IN$_{a}$ populations were similar in magnitude and did not appear to be influenced by sex or age. The enhancement of FS-IN$_{na}$ excitability was maintained across adult life, but the weak correlation ($r^2 = 0.19$) we observed within this smaller dataset ($n = 8$) was not significant (Fig. 5*E*). As expected, no change in the excitability of the FS-IN$_{a}$

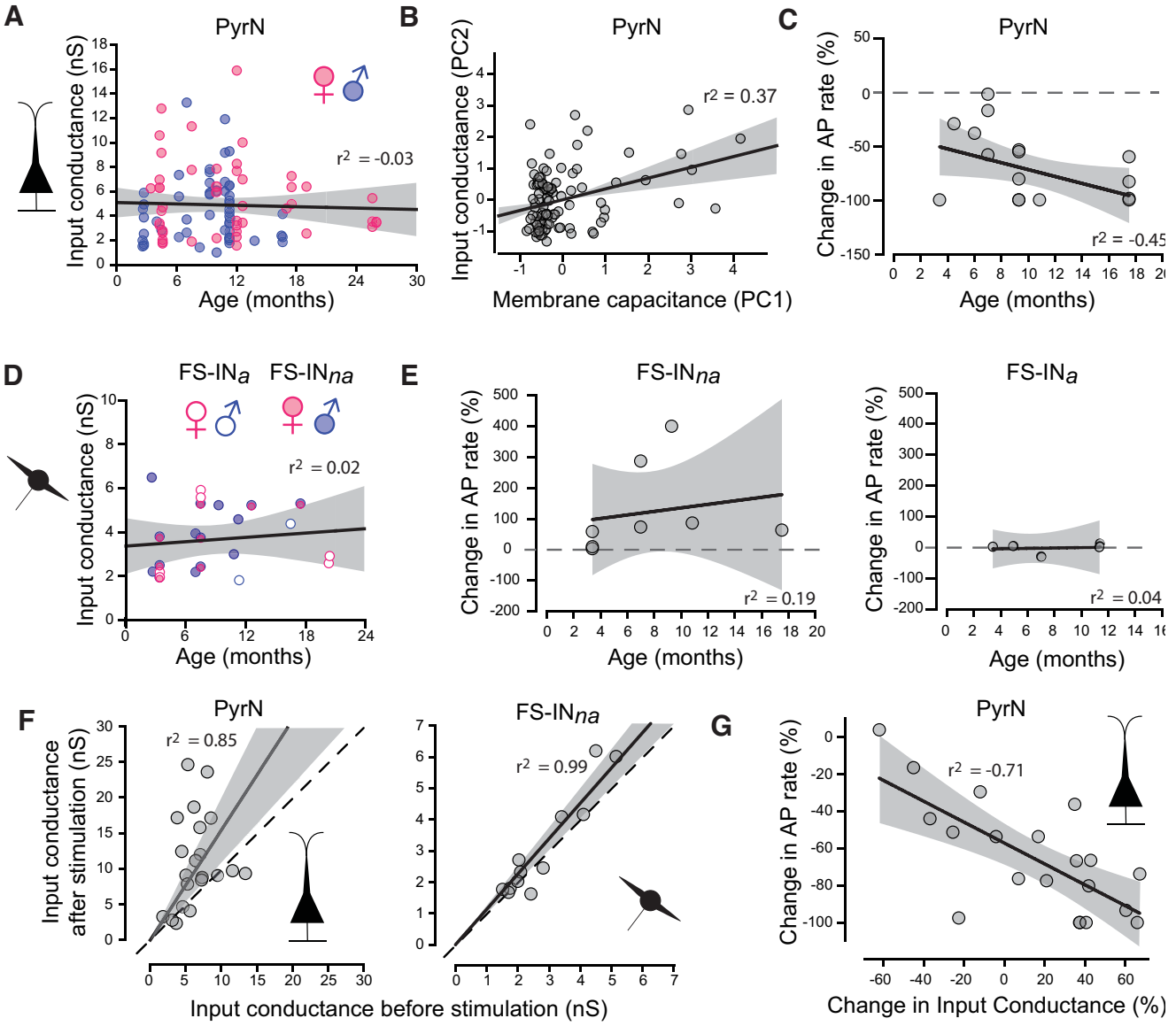

Figure 5. Age-related and sex-related differences in PFC excitability. ***A***, Scatter plot of the resting input conductance taken from all PyrNs recorded from mice 3–27 months of age. These data are separated into male (blue circles) and female (pink circles). The solid line is the result of linear regression analysis of the combined male and female data demonstrating a lack of change in input conductance across the adult life span. The gray-shaded area shows the 95% confidence level for this fit, and the r^2 value of −0.03 indicates how little of the variability in resting excitability can be explained by age. ***B***, Normalized data comparing the relationship between the membrane capacitance (PC1) and the input conductance (PC2) for all PyrNs recorded across all ages. The linear regression analysis demonstrates that there is a relationship between these two parameters. ***C***, Changes in AP rate obtained from PyrN recordings are plotted in relation to the age of the animal. The results of linear regression analysis are superimposed on this scatter plot, demonstrating a relationship between the strength of the inhibition and the age of the animal. ***D***, Scatter plot of data from FS-IN cells. Measurements from FS-IN$_a$s and FS-IN$_{na}$s have been separated into male and female, but once again the linear region indicates that the resting excitability of FS-INs does not vary across the adult life span. ***E***, Changes in AP rate obtained from interneuron recordings are plotted in relation to the age of the animal. The results of linear regression analysis are superimposed on scatter plots obtained for the FS-IN$_{na}$ and the FS-IN$_a$ populations. ***F***, Scatter plots of the resting input conductance measured before and after TMN$_{HDC}$ optogenetic stimulation. The dashed line has a slope of 1 to illustrate the enhancement of the input conductance that is apparent for the PyrN recordings but not the FS-IN$_{na}$ population. ***G***, The change in AP rate data shown in ***C*** was replotted in relation to the change in input conductance for each PyrN. Once again, the results of linear regression analysis are superimposed on this scatter plot. The significant negative correlation ($p = 0.0004$) shows that larger increases in input conductance are associated with greater reduction in AP rate within the PyrN population.

population ($n = 5$) was observed at any of the ages examined in this study (Fig. 5*E*).

Consistent with modulation of a tonic GABA$_A$ receptor-mediated conductance following GABA release from TMN$_{HDC}$ axons, we observed a clear enhancement of the resting input conductance in PyrNs that followed the same time course as the reduction in AP firing (data not shown). Following TMN$_{HDC}$ activation, the input conductance increased from 6.52 ± 2.16 to 11.85 ± 1.65 nS (Fig. 5*F*). In contrast, no significant change was observed for the FS-IN$_{na}$ population with a resting input conductance of 2.79 ± 0.35 nS before stimulation and 3.07 ± 0.48 nS after stimulation (Wilcoxon signed-rank test, $p = 0.1$). The increase in the input conductance of PyrNs correlated with the magnitude of the reduction in AP firing, as shown by the linear regression analysis of the normalized data (Fig. 5*G*), with an r^2 value for this fit of −0.71 with a slope that was significantly different from zero (ANOVA, $p = 0.0004$). Therefore, the age-related changes we observed following TMN$_{HDC}$ modulation of AP firing can be explained by enhanced modulation of the input conductance.

Discussion

This study demonstrates how histamine/GABA released from TMN_{HDC} axons alters AP firing within the mouse PFC in a cell-specific and age-specific manner. We recorded from three distinct classes of PFC neuron in PL, AC, and IL regions of the PFC: layer 2/3 PyrNs, FS-IN_{na}s, and FS-IN_as. Each cell type responded differently to optogenetic stimulation of TMN_{HDC} axons. The AP firing of the FS-IN_a population was unaltered, while the FS-IN_{na} population (putative parvalbumin-positive cells) was excited and the PyrN population was robustly inhibited (Fig. 6, conceptual summary). Pharmacological experiments confirmed that histamine release was responsible for FS-IN_{na} excitation, whereas the GABA release from THN_{HDC} axons was responsible for the inhibition of PyrNs. By making recordings from mice over the adult life span (3–27 months postnatally), we found that shunting inhibition produced by GABA modulation was more pronounced in the adult and was sustained into older age.

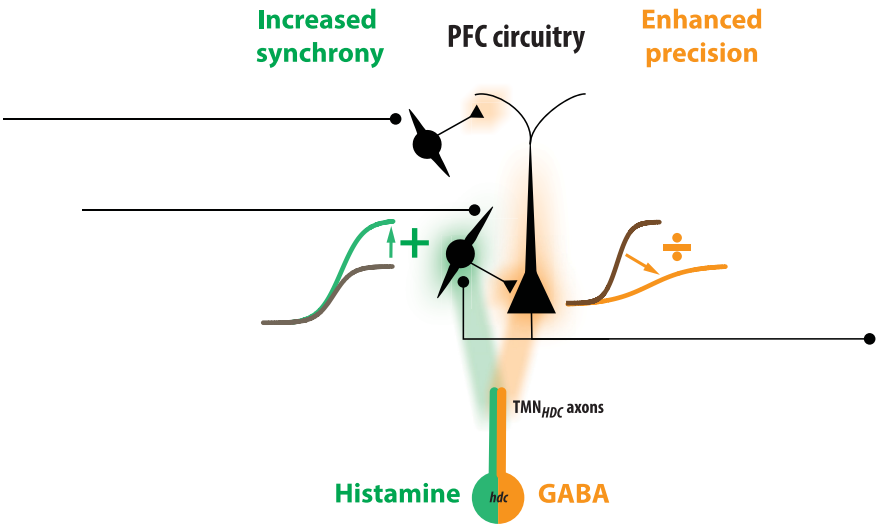

Figure 6. Summary of salient features associated with TMN modulation of the PFC. Illustration that highlights the actions of the histamine (green) and GABA (orange) released from TMN_{HDC} axons. The GABA released from TMN_{HDC} axons will lead to enhanced precision and greater dynamic range within the PFC because of the divisive gain change produced within the PyrNs. In parallel, the histamine released from TMN_{HDC} axons will increase synchrony within the PFC network because of the additive gain change associated with the FS-IN_{na} population.

Although the net effect of the wake-promoting histamine system in the brain is excitatory at the behavioral level (Haas and Panula, 2003; Scammell et al., 2019; Yoshikawa et al., 2021), in the case of the neocortical network we propose that the histamine-GABA system influences the requirement of the circuit for AP precision. On the one hand, we find that histamine stimulates a subset of fast-spiking GABAergic interneurons that will increase phasic inhibition in PyrNs to enhance the precision of PyrNs and expand their dynamic range to enhance synchrony in the PFC network (Krimer et al., 2005; Feldmeyer et al., 2018). On the other hand, the raised ambient GABA levels produced following TMN_{HDC} axon GABA release will speed up the membrane time constant of PyrNs by enhancing the resting input conductance following extrasynaptic $GABA_A$ receptor activation and, therefore, will also enhance coincidence detection, such that more closely timed EPSP inputs will be required to elicit APs (Brickley and Mody, 2012; Wlodarczyk et al., 2013; Sylantyev et al., 2020). By limiting the window of coincidence detection, tonic inhibition can promote conditions that enhance cognition. Moreover, we propose that the additive gain changes associated with the FS-IN_{na} population of the PFC will further promote synchrony of the network during wakefulness.

Previously, gain changes within neocortical circuits were studied in relation to the action of neuromodulators such as serotonin and acetylcholine on interneurons (Ferguson and Cardin, 2020). However, this is different from the mechanism we propose, whereby GABA release from TMN_{HDC} axons is directly responsible for the generation of a shunting inhibition (Fig. 6). Within minutes of TMN_{HDC} optoactivation, the PyrN population experienced a dramatic reduction in the slope of the input–output relationship and a reduction in the maximum AP firing rate. As expected, this divisive gain change was associated with a significant 20% increase in the input conductance, with no change in the RMP, a characteristic of a tonic shunting inhibition mediated by extrasynaptic $GABA_A$ receptors (Mitchell and Silver, 2003). Therefore, GABA diffusion through the extracellular space is sufficiently unhindered to enable rapid coupling between the GABA released from TMN_{HDC} axons and alterations in the gain of the surrounding PyrNs. This is similar to the mode of action reported in other cortical and striatal regions following TMN_{HDC} activation (Yu et al., 2015) and consistent with observations following the knockout of high-affinity δ-subunit-containing $GABA_A$ receptors (Abdurakhmanova et al., 2020). The lack of a shunting inhibition observed in FS-IN_{na} and FS-IN_a populations would suggest that the change in GABA levels produced following release from TMN_{HDC} axons was insufficient to activate extrasynaptic $GABA_A$ receptors on these cells.

We have investigated the consequence of TMN_{HDC} activation for local interneuron excitability and observed an increase in the gain of these neurons, but this gain change was predominantly additive, and the time course of the response was much slower than that observed for PyrNs. In contrast to the effects of TMN_{HDC} activation on PyrNs, the additive gain change observed for the FS-IN_{na} population was because of the actions of histamine on H1/H2 receptors. The delayed increase in FS-IN_{na} excitability is consistent with the reduction of an outward potassium conductance that was reported in hippocampal interneurons following H2 receptor activation and subsequent coupling to adenylate cyclase pathways (Atzori et al., 2000). The delayed nature of this excitability change is also consistent with the role of histamine release from TMN axons in maintaining wakefulness more than switching behavioral states (Takahashi et al., 2006). Moreover, the slow time course of the histamine effects on FS-IN_{na} populations suggest that these changes will be sustained compared with the shunting inhibition observed for PyrNs. Future studies are clearly required to understand the interactions more fully between the actions of histamine and GABA in the PFC. However, what is clear from our data is that the divisive gain change that results from the direct actions of TMN_{HDC} axon-released GABA in extrasynaptic $GABA_A$ receptors dominates in the PFC, as this still occurs in the presence of H1/H2 receptor blockers when the excitability of surrounding interneurons was not altered. This result demonstrates that the shunting inhibition is largely because of the release of GABA from the TMN_{HDC}

axons and is not greatly influenced by increased GABA release from local interneurons.

Human brain-imaging studies have reported lower levels of variability in the resting-state BOLD signal in the PFC of individuals in later life (Nomi et al., 2017), and this reduction in signal variability has been associated with overall decreased GABA levels in the cortex (Porges et al., 2021). In older humans, positive allosteric modulation of γ2-subunit-containing $GABA_A$ receptors, for example with lorazepam, may protect against cognitive decline (Lalwani et al., 2021). Tonic inhibition can come from GABA activation of both γ2- and δ-subunit-containing receptors, but only γ2-subunit-containing $GABA_A$ receptor-mediated responses can be allosterically enhanced by benzodiazepines. Similarly, for individuals who maintain cognitive performance with aging, the increases in TMN_{HDC} GABA modulation of PyrNs during aging may be an adaptive mechanism to buttress cognition.

Finally, we note that our present and previous results on GABA-histamine corelease do differ from results reported in another study (Venner et al., 2019). In general, most findings, whether pharmacological or genetic, support the role of histamine in promoting wakefulness, although, as usually found, permanent gene or cell knockouts/lesions tend to give different results from reversible pharmacology or knockdowns: for example, *hdc* gene knockouts and *hdc* cell lesions induce sleep–wake fragmentation (insomnia), but do not affect overall levels of sleep–wake (Parmentier et al., 2002; Yu et al., 2019); on the other hand, in histamine H1 receptor antagonists, chemogenetic or optoinhibition of histamine neurons induces non-rapid eye movement-like sleep (Fujita et al., 2017; Yu et al., 2019; Naganuma et al., 2021; Yoshikawa et al., 2021). We have previously explored how levels of arousal are altered following chemogenetic manipulation of this TMN_{HDC} projection (Yu et al., 2015) and found that activation of the TMN_{HDC} projection increased motor activity, and that genetic knockdown of *vgat* from this pathway sustains wakefulness. In contrast, Venner et al. (2019) reported that chemogenetic manipulation of *hdc* cells did not affect sleep–wake behavior and found no role for GABA in wakefulness (Venner et al., 2019; Arrigoni and Fuller, 2021). However, the Cre line used by Venner et al. (2019) does not target all *hdc*-expressing neurons. For our mechanism of GABA release, we propose the mechanism is via VGAT (Yu et al., 2015); but, in any case, GABA can also be transported into synaptic vesicles by the vesicular monoamine transporter VMAT (Tritsch et al., 2012), whose gene is strongly expressed in histaminergic cells (Mickelsen et al., 2020). Venner et al. (2019) did not provide electrophysiological evidence to support their contention that GABA was not released from TMN_{HDC} axons in the neocortex, although they found using slice electrophysiology that histamine axons projecting to the preoptic hypothalamus did not release GABA. The best explanation for the disparities between studies are that the various subtypes of histamine neurons identified by RNAseq studies differ in their ability to release GABA (Mickelsen et al., 2020).

In summary, we present evidence that histamine released from TMN_{HDC} axons is responsible for additive gain change within specific interneuron populations of the adult PFC. We speculate in Figure 6 that these changes in FS-IN_{na} excitability will lead to increased synchronization of cortical circuitry of the type (high frequency) associated with the awake brain (Yu et al., 2015). In contrast, the GABA released from these same TMN_{HDC} axons leads to a divisive gain change that will broaden the dynamic range of PyrNs (Fig. 6), a feature that will lead to greater computational flexibility within the PFC. We have also shown that the shunting inhibition associated with GABA release increases with age, and it is intriguing to speculate that enhancement of this feature of TMN_{HDC} modulation could be a compensation for age-related declines in global GABA levels observed within the PFC (Porges et al., 2021). Enhanced GABA modulation from TMN_{HDC} axons could protect against reduced cognitive flexibility that is a feature of the aging process, while histamine release will support arousal because of the modulation of local interneurons.

References

Abdurakhmanova S, Grotell M, Kauhanen J, Linden AM, Korpi ER, Panula P (2020) Increased sensitivity of mice lacking extrasynaptic δ-containing $GABA_A$ receptors to histamine receptor 3 antagonists. Front Pharmacol 11:594.

Airaksinen MS, Panula P (1988) The histaminergic system in the guinea pig central nervous system: an immunocytochemical mapping study using an antiserum against histamine. J Comp Neurol 273:163–186.

Airaksinen MS, Alanen S, Szabat E, Visser TJ, Panula P (1992) Multiple neurotransmitters in the tuberomammillary nucleus: comparison of rat, mouse, and guinea pig. J Comp Neurol 323:103–116.

Arrigoni E, Fuller PM (2021) The role of the central histaminergic system in behavioral state control. Curr Top Behav Neurosci 59:447–468.

Atzori M, Lau D, Tansey EP, Chow A, Ozaita A, Rudy B, McBain CJ (2000) H2 histamine receptor-phosphorylation of Kv3.2 modulates interneuron fast spiking. Nat Neurosci 3:791–798.

Bolam JP, Ellender TJ (2016) Histamine and the striatum. Neuropharmacology 106:74–84.

Brickley SG, Mody I (2012) Extrasynaptic GABA(A) receptors: their function in the CNS and implications for disease. Neuron 73:23–34.

Brickley SG, Cull-Candy SG, Farrant M (1996) Development of a tonic form of synaptic inhibition in rat cerebellar granule cells resulting from persistent activation of GABAA receptors. J Physiol 497:753–759.

Brickley SG, Revilla V, Cull-Candy SG, Wisden W, Farrant M (2001) Adaptive regulation of neuronal excitability by a voltage-independent potassium conductance. Nature 409:88–92.

Brickley SG, Franks NP, Wisden W (2018) Modulation of GABA-A receptor function and sleep. Curr Opin Physiol 2:51–57.

Ellender TJ, Huerta-Ocampo I, Deisseroth K, Capogna M, Bolam JP (2011) Differential modulation of excitatory and inhibitory striatal synaptic transmission by histamine. J Neurosci 31:15340–15351.

Feldmeyer D, Qi G, Emmenegger V, Staiger JF (2018) Inhibitory interneurons and their circuit motifs in the many layers of the barrel cortex. Neuroscience 368:132–151.

Ferguson KA, Cardin JA (2020) Mechanisms underlying gain modulation in the cortex. Nat Rev Neurosci 21:80–92.

Fujita A, Bonnavion P, Wilson MH, Mickelsen LE, Bloit J, de Lecea L, Jackson AC (2017) Hypothalamic tuberomammillary nucleus neurons: electrophysiological diversity and essential role in arousal stability. J Neurosci 37:9574–9592.

Haas H, Panula P (2003) The role of histamine and the tuberomamillary nucleus in the nervous system. Nat Rev Neurosci 4:121–130.

Haas HL, Panula P (2016) Histamine receptors. Neuropharmacology 106:1–2.

Hippenmeyer S, Vrieseling E, Sigrist M, Portmann T, Laengle C, Ladle DR, Arber S (2005) A developmental switch in the response of DRG neurons to ETS transcription factor signaling. PLoS Biol 3:e159.

Joseph DR, Sullivan PM, Wang YM, Kozak C, Fenstermacher DA, Behrendsen ME, Zahnow CA (1990) Characterization and expression of the complementary DNA encoding rat histidine decarboxylase. Proc Natl Acad Sci U|S|A 87:733–737.

Krimer LS, Zaitsev AV, Czanner G, Kröner S, González-Burgos G, Povysheva NV, Iyengar S, Barrionuevo G, Lewis DA (2005) Cluster analysis-based physiological classification and morphological properties of inhibitory neurons in layers 2-3 of monkey dorsolateral prefrontal cortex. J Neurophysiol 94:3009–3022.

Kukko-Lukjanov TK, Panula P (2003) Subcellular distribution of histamine, GABA and galanin in tuberomamillary neurons in vitro. J Chem Neuroanat 25:279–292.

Lalwani P, Garrett DD, Polk TA (2021) Dynamic recovery: GABA agonism restores neural variability in older, poorer performing adults. J Neurosci 41:9350–9360.

Lee V, Maguire J (2014) The impact of tonic GABAA receptor-mediated inhibition on neuronal excitability varies across brain region and cell type. Front Neural Circuits 8:3.

Ma S, Hangya B, Leonard CS, Wisden W, Gundlach AL (2018) Dual-transmitter systems regulating arousal, attention, learning and memory. Neurosci Biobehav Rev 85:21–33.

McIntire SL, Reimer RJ, Schuske K, Edwards RH, Jorgensen EM (1997) Identification and characterization of the vesicular GABA transporter. Nature 389:870–876.

Mickelsen LE, Flynn WF, Springer K, Wilson L, Beltrami EJ, Bolisetty M, Robson P, Jackson AC (2020) Cellular taxonomy and spatial organization of the murine ventral posterior hypothalamus. Elife 9:e58901.

Mitchell SJ, Silver RA (2003) Shunting inhibition modulates neuronal gain during synaptic excitation. Neuron 38:433–445.

Naganuma F, Nakamura T, Kuroyanagi H, Tanaka M, Yoshikawa T, Yanai K, Okamura N (2021) Chemogenetic modulation of histaminergic neurons in the tuberomamillary nucleus alters territorial aggression and wakefulness. Sci Rep 11:17935.

Nomi JS, Bolt TS, Ezie CEC, Uddin LQ, Heller AS (2017) Moment-to-moment BOLD signal variability reflects regional changes in neural flexibility across the lifespan. J Neurosci 37:5539–5548.

Panula P, Yang HY, Costa E (1984) Histamine-containing neurons in the rat hypothalamus. Proc Natl Acad Sci U|S|A 81:2572–2576.

Parmentier R, Ohtsu H, Djebbara-Hannas Z, Valatx JL, Watanabe T, Lin JS (2002) Anatomical, physiological, and pharmacological characteristics of histidine decarboxylase knock-out mice: evidence for the role of brain histamine in behavioral and sleep-wake control. J Neurosci 22:7695–7711.

Porges EC, Jensen G, Foster B, Edden RA, Puts NA (2021) The trajectory of cortical GABA across the lifespan, an individual participant data meta-analysis of edited MRS studies. Elife 10:e62575.

Scammell TE, Jackson AC, Franks NP, Wisden W, Dauvilliers Y (2019) Histamine: neural circuits and new medications. Sleep 42:

Senba E, Daddona PE, Watanabe T, Wu JY, Nagy JI (1985) Coexistence of adenosine deaminase, histidine decarboxylase, and glutamate decarboxylase in hypothalamic neurons of the rat. J Neurosci 5:3393–3402.

Sylantyev S, Savtchenko LP, O'Neill N, Rusakov DA (2020) Extracellular GABA waves regulate coincidence detection in excitatory circuits. J Physiol 598:4047–4062.

Takagi H, Morishima Y, Matsuyama T, Hayashi H, Watanabe T, Wada H (1986) Histaminergic axons in the neostriatum and cerebral cortex of the rat: a correlated light and electron microscopic immunocytochemical study using histidine decarboxylase as a marker. Brain Res 364:114–123.

Takahashi K, Lin JS, Sakai K (2006) Neuronal activity of histaminergic tuberomammillary neurons during wake-sleep states in the mouse. J Neurosci 26:10292–10298.

Takeda N, Inagaki S, Shiosaka S, Taguchi Y, Oertel WH, Tohyama M, Watanabe T, Wada H (1984) Immunohistochemical evidence for the coexistence of histidine decarboxylase-like and glutamate decarboxylase-like immunoreactivities in nerve cells of the magnocellular nucleus of the posterior hypothalamus of rats. Proc Natl Acad Sci U|S|A 81:7647–7650.

Tritsch NX, Ding JB, Sabatini BL (2012) Dopaminergic neurons inhibit striatal output through non-canonical release of GABA. Nature 490:262–266.

Trottier S, Chotard C, Traiffort E, Unmehopa U, Fisser B, Swaab DF, Schwartz JC (2002) Co-localization of histamine with GABA but not with galanin in the human tuberomamillary nucleus. Brain Res 939:52–64.

Venner A, Mochizuki T, De Luca R, Anaclet C, Scammell TE, Saper CB, Arrigoni E, Fuller PM (2019) Reassessing the role of histaminergic tuberomammillary neurons in arousal control. J Neurosci 39:8929–8939.

Wall MJ (2002) Furosemide reveals heterogeneous GABA(A) receptor expression at adult rat Golgi cell to granule cell synapses. Neuropharmacology 43:737–749.

Watanabe T, Taguchi Y, Hayashi H, Tanaka J, Shiosaka S, Tohyama M, Kubota H, Terano Y, Wada H (1983) Evidence for the presence of a histaminergic neuron system in the rat brain: an immunohistochemical analysis. Neurosci Lett 39:249–254.

Wlodarczyk AI, Xu C, Song I, Doronin M, Wu YW, Walker MC, Semyanov A (2013) Tonic GABAA conductance decreases membrane time constant and increases EPSP-spike precision in hippocampal pyramidal neurons. Front Neural Circuits 7:205.

Yoshikawa T, Nakamura T, Yanai K (2021) Histaminergic neurons in the tuberomammillary nucleus as a control centre for wakefulness. Br J Pharmacol 178:750–769.

Yu X, Ye Z, Houston CM, Zecharia AY, Ma Y, Zhang Z, Uygun DS, Parker S, Vyssotski AL, Yustos R, Franks NP, Brickley SG, Wisden W (2015) Wakefulness is governed by GABA and histamine cotransmission. Neuron 87:164–178.

Yu X, Ma Y, Harding EC, Yustos R, Vyssotski AL, Franks NP, Wisden W (2019) Genetic lesioning of histamine neurons increases sleep-wake fragmentation and reveals their contribution to modafinil-induced wakefulness. Sleep 42:zsz031.

Zecharia AY, Yu X, Götz T, Ye Z, Carr DR, Wulff P, Bettler B, Vyssotski AL, Brickley SG, Franks NP, Wisden W (2012) GABAergic inhibition of histaminergic neurons regulates active waking but not the sleep-wake switch or propofol-induced loss of consciousness. J Neurosci 32:13062–13075.